Title

Fracture detection and imaging through relative seismic velocity changes using distributed acoustic sensing and ambient seismic noise

Journal

The Leading Edge, 36(12)

ISSN

1070-485X

Authors

James, Stephanie R
Knox, Hunter A
Preston, Leiph
et al.

Publication Date

2017-12-01

DOI

10.1190/tle36121009.1

Peer reviewed

Fracture detection and imaging through relative seismic velocity changes using distributed acoustic sensing and ambient seismic noise

Keywords: crosscorrelation, crosswell, distributed systems, fiber-optic sensors, fracture stimulation

Stephanie R. James[12], Hunter A. Knox[2], Leiph Preston[2], James M. Knox[2], Mark C. Grubelich[2], Dennis K. King[2], Jonathan B. Ajo-Franklin[3], Tim C. Johnson[4] and Joseph P. Morris[5]

1 University of Florida.

2 Sandia National Laboratories.

3 Lawrence Berkeley National Laboratory.

4 Pacific Northwest National Laboratory.

5 Lawrence Livermore National Laboratory.

Corresponding author: sjames@usgs.gov

Abstract

Fracture systems are important pathways for fluid and solute transport and exert a critical influence on the hydraulic properties of aquifers and reservoirs. Therefore, detailed knowledge of fracture locations, connections, and evolution is crucial for both groundwater and energy applications (e.g., enhanced geothermal, oil and gas recovery, carbon sequestration, and wastewater injection). The innovative combination of distributed acoustic sensing (DAS) and ambient seismic noise techniques has the potential to detect and characterize fracture systems at high-spatial and temporal resolution without an active source. To test this, we conducted a multiphysics field experiment at Blue Canyon Dome, New Mexico. A novel energetic material developed by Sandia National Laboratories was used to generate fractures in two separate stimulations. Ambient noise was recorded before and after each stimulation using fiber-optic cables installed in the outer annulus of four boreholes surrounding the stimulation hole at a radius of 1.2 m. The Python package MSNoise was used to compute crosscorrelations and measure changes in velocity between each time period relative to the initial (prestimulation) time period. The majority of channel pairs showed a velocity reduction (average −3% relative velocity change) following both stimulations. We used a 3D Bayesian tomography approach to resolve spatial variations by utilizing differences between channel pairs. Results showed that the greatest velocity reduction was concentrated near the center of the test area and suggested the presence of a near-vertical fracture, oriented northeast to southwest for depths >19 m below ground surface and extending slightly to the southwest corner. These results were generally consistent with crosshole seismic tomography time-lapse images. DAS technology provides valuable sensing capability and — when used with

a passive seismic approach — shows great promise for monitoring and characterization of fractured-rock systems.

Permalink: https://doi.org/10.1190/tle36121009.1

Keywords: crosscorrelation, crosswell, distributed systems, fiber-optic sensors, fracture stimulation

While it is well known that fracture networks provide essential pathways for fluid and solute transport, the complexity of their generation, evolution, and morphology continues to be a challenge for characterization and monitoring (National Research Council, 1996; Berkowitz, 2002; Neuman, 2005). The intricate heterogeneity and anisotropy of fractured systems remain important obstacles for hydrogeologic studies and energy extraction (e.g., enhanced geothermal systems and tight shale-gas reservoirs). Accurate characterization of fracture extent, orientation, and communication is needed for assessing hydraulic properties and, subsequently, to provide direction to decision makers concerning safe and sustainable extraction and injection efforts.

Borehole and surficial geophysical methods have been used successfully for characterization (e.g., Verdon et al., 2009; Day-Lewis et al., 2017), but they encounter limitations in efficiency and spatial resolution due to the multiscale nature of fracture networks. Fracture apertures are typically small (microns to centimeters) but extend over large areas (meters to tens of meters) (Geertsma and De Klerk, 1969; Johns et al., 1993; Hakami and Larsson, 1996). Fracture systems with small apertures and density are typically unresolvable without a drill-back or mine-back study (Warpinski and Teufel, 1987). Borehole logging and crosshole methods allow for detailed interrogation of the subsurface at very fine scales and up to four dimensions (e.g., Tsvankin et al., 2010). However, this level of detail requires lengthy campaign-style surveying and reoccupation and comes at great expense, with construction of additional boreholes and possibly permanent installation of geophysical sensors. Ideally, a compromise can be reached where geophysical monitoring could be performed with a suite of inexpensive sensors in a crosshole geometry within nominally uncompleted boreholes (i.e., open below-surface casing). This would allow targeting a zone of interest from multiple azimuths and close offsets, which would improve both spatial and temporal resolution (i.e., multiphysics with large numbers of sensors [“large N”] approaches such as in Neal and Krohn [2012] and Bergmann et al. [2014]).

Distributed-sensing technologies represent a promising tool for multiphenomenological investigations, especially for fracture-flow systems where measuring acoustic, strain, and temperature signals is important. These sensing technologies offer the opportunity for large N permanent installations (i.e., either grouted behind casing or direct buried) at lower economic burdens since the fiber cost is relatively low. Further, fiber-based methods provide distributed measurements with offsets tailored to the

project's scale, typically on the order of a few meters. The three primary challenges for this type of monitoring are (1) the large volumes of data that are recorded with these extensive arrays, (2) the differences in sensitivity and directionality of fibers in contrast with conventional point sensors, and (3) the cost of the interrogator systems. The first challenge is addressed through the ever-increasing availability of computational power and data storage, while the latter two will only be addressed as fiber-based measurements become more commonplace and well characterized. For the remainder of the paper, we will focus only on distributed acoustic sensing (DAS) and an application that could further reduce the economic burden of long-term monitoring by eliminating active sources as a requirement for change-detection imaging.

DAS is a new and rapidly advancing technology that uses fiber-optic cables to detect the transmission of acoustic waves through the subsurface (Molenaar et al., 2012; Daley et al., 2013; Parker et al., 2014). An interrogator box sends a laser pulse through the cable and records as minor imperfections cause a portion of the light to be backscattered through Rayleigh scattering. Passing acoustic waves stretch and compress the cable, thereby altering the optical path length and subsequent traveltime of the backscattered light. Scattering occurs along the entire length of cable, allowing for a distributed network of individual channels (or sensors). However, only the scatterers in the perturbed portion of fiber will show a change in transit time, thereby allowing for their spatial isolation. Application of this method within boreholes has the potential to provide detailed information on fracture geometries and characteristics by monitoring changes in seismic velocity. This could be particularly valuable for providing actionable feedback during injection and extraction operations, assuming adequate inversion algorithms exist.

Seismic interferometry using ambient seismic noise is another burgeoning field that has great potential for passive monitoring applications. Crosscorrelation of records from two stations is effective at estimating the impulse response, or empirical Green's function, of the media between the two stations (Campillo and Paul, 2003; Shapiro and Campillo, 2004). The first station becomes a virtual source for the waves recorded on the second. This technique has been applied successfully for a variety of applications from crustal to near-surface scales (e.g., Moschetti et al., 2007; Picozzi et al., 2009; James et al., 2017). However, ambient-noise studies are limited in their depth of investigation and spatial resolution by the sensor spacing. Therefore, DAS technology could be a boon for seismic interferometry studies since it transforms a continuous line of fiber-optic cable (meters to kilometers in length) into a distributed network of sensors at very close spacing (~1 m). Here, we present results from a unique field experiment in which we used DAS installed in the annulus of four monitoring boreholes to record the ambient-noise wavefield before and after fracture emplacement from a novel energetic material. Specifically, DAS was examined for its

potential in fracture-generation detection and fracture imaging, as well as to provide a unique data set for examining the ambient wavefield as recorded by DAS within boreholes.

We conducted this field experiment as part of the Department of Energy Subsurface Science, Technology, Engineering, and R&D (SubTER) crosscut with the goal of developing efficient and economic systems for imaging and monitoring fractures. While multiple geophysical characterization and change-detection techniques were applied (Knox et al., 2016), this paper focuses on the utilization of DAS, ambient-noise interferometry, and seismic change-detection techniques for fracture imaging. We present tomographic results from the more established crosshole seismic logging (CSL) active-source survey for comparison. Even though these two seismic methods were sensitive to different feature scales and the inversion approaches differed, a first-order comparison for determining successful fracture detection and delineation was valuable. The experimental design consisted of five boreholes drilled to 23 m below ground surface configured in a five-spot borehole pattern. A center stimulation hole (C, center) was surrounded by four cased monitoring holes at a radius of 1.2 m (4 ft) and oriented along the cardinal directions (N1, north-1; E2, east-2; S3, south-3; and W4, west-4) (Figure 1). These monitoring holes were instrumented with electrodes and fiber-optic cables attached to the outside of the casing and grouted in place (Figure 2a). We used a single continuous fiber-optic cable for all four monitoring holes, starting in the west hole and ending in the north, with each hole containing a downgoing and upgoing segment.

Figure 1. (a) This study was conducted at Blue Canyon Dome, approximately 120 km south of Albuquerque, New Mexico. (b) The monitoring boreholes were configured in a five-spot borehole pattern oriented north-south and east-west, with a stimulation borehole located in the center.

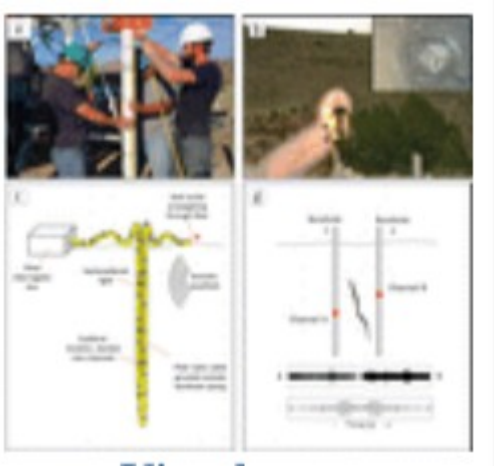

Figure 2. (a) The downgoing and upgoing portions of the fiber-optic cable were grouped and attached to the outside of the borehole casings. (b) An example image of the second stimulation is shown along with an inset photo from the downhole camera at 15 m of the near-vertical fracture generated. (c) Conceptual model of the DAS collection scheme: The Silixa iDAS interrogator box sends a laser pulse through the fiber every 100 μs. Postprocessing results in scatterer locations (seismic channels) every ~1 m. (d) Conceptual model of the crosscorrelation analysis: Recordings from channels within separate boreholes, and less than 60° vertical offset, were crosscorrelated to return the impulse response of the subsurface between the two channels. Channel pairs spanning the generated fracture should experience a stronger velocity change than pairs that do not intercept the fracture, thereby allowing for detection and possible delineation of the fracture location.

Upon completion of the boreholes, the field campaign began with geophysical characterization of the site using seismic and electrical methods, which established the test bed's initial conditions. The next step was to emplace a fracture network using a novel energetic material developed by Sandia National Laboratories, which allowed us to eliminate near-field wellbore damage by tailoring the initial pressure while creating an extended pressure pulse to drive the multiple energetically initiated fractures. This energetic stimulation technique bridges the gap between a propellant and a conventional high-explosive stimulation. Minimal damage was caused to the stimulation hole, thereby allowing reentry for repeated tests. The energetic material was emplaced between 18 and 22 m depth in the open hole section of the center stimulation borehole. Afterward, another comprehensive characterization effort was undertaken using hydrologic tests, geophysical tracers, seismic, and electrical methods. The stimulation borehole was then refractured using the same novel energetic material to test the efficacy of secondary stimulation. The test bed underwent a final comprehensive hydrologic and geophysical characterization. These series of measurements afforded detailed investigations into fracturing, refracturing, and flow phenomenology (Knox et al., 2016). DAS and crosshole seismic measurements were taken throughout at targeted intervals.

Study site. The field test was conducted at Blue Canyon Dome, which is located ~6 km west of Socorro, New Mexico, on a ridge shared with Socorro Peak (Figure 1). The site is managed by the Energetic Materials Research and Testing Center, an affiliation of the New Mexico Institute of Mining and Technology. The ridge is unbounded on three sides and free of background

stress that might generate preferential fracture orientations. The shallow configuration of the wells also precludes the site from having strong preferential stress directions. The site geology consists dominantly of Miocene-age rhyolite (Chamberlin, 1981).

Borehole logging provided details on the lithology, texture, preexisting fractures, and borehole construction. A weathering contact occurs at ~9 m depth separating weathered and highly fractured rhyolite above from comparatively unweathered rhyolite below. Sparse near-vertical and remineralized fractures were observed at deeper depths (>9 m). A zone of larger clast sizes was observed in the optical televiewer logs near the bottom of the boreholes. Gamma-gamma logs indicated a single lithology throughout with little clay. Caliper logs showed the boreholes were consistently sized (13 cm) with no or minimal drilling-induced fractures (Knox et al., 2016). Deviation logs indicated the boreholes had minor titling (<2°) and deviation (<0.2 m). However, the close hole spacing made the *x*-*y* deviations significant, so all measurement locations were corrected to account for this deviation.

DAS and ambient seismic noise. Crosscorrelations of ambient seismic noise are useful for measuring subtle changes in seismic velocity in the subsurface between two stations (e.g., Sens-Schönfelder and Wegler, 2006; Brenguier et al., 2011). Comparison of the scattered arrivals within crosscorrelations between two time periods allows for measurement of the change in velocity relative to the earlier time. The presence of fractures typically reduces bulk seismic velocity (Moos and Zoback, 1983). Therefore, the emplacement of fractures at Blue Canyon Dome was expected to result in a measurable reduction in seismic velocity as recorded in the ambient-noise wavefield. Fractures should also alter traveltimes through increased scattering. Seismic waves traveling perpendicular to fractures were expected to experience stronger velocity reductions than waves that intercept only a small portion or none of the fracture (Figure 2). Therefore, variations between different channel pairs should be useful for detecting the fracture location and orientation.

We installed a continuous length of fiber-optic cable (tactical single-mode/multimode cable with polyurethane sheathing) behind casing in the monitoring boreholes (Figure 2). The fiber was grouted in place, which allowed for repeat collection of passive and active seismic data throughout the study. Silixa was contracted to collect the DAS recordings using their iDAS system and a 10 m gauge length. Approximately 13 hours of ambient seismic noise were recorded before and after each energetic stimulation creating four distinct time periods for comparison: pre- and poststimulation 1 and pre- and poststimulation 2. Poststimulation 1 and prestimulation 2 data were treated as distinct because large volumes of fluid (water and tracers) were injected into the system at low pressures (≤70 psi) between the two stimulations. Ambient recordings occurred approximately between 6:30 p.m. and 7:30 a.m. to minimize potentially dominant influences from on-site

activities. Environmental and anthropogenic noise sources were expected, though the specific sources were not known, nor was knowledge of their origin required for the crosscorrelation procedure. Silixa completed the denoising and preprocessing stacking of scatterers to create ~1 m channel spacing.

Processed data consisted of HDF5 files containing 30 s records, at 10 kHz sampling rate, for all 263 channels. Each ~13-hour time period resulted in ~500 Gb of data, totaling nearly 2 Tb of continuous data. Once the data were compiled, we determined the channel depths and locations corresponding to each borehole, removed all aboveground channels, and corrected locations using the deviation logs. To make the large data set more manageable, and analysis computationally feasible, we focused only on channels located within the unweathered rhyolite zone (>9 m depth) and further downsampled by a factor of 3. This resulted in a final 60 channels, with ~3 m spacing, the records of which we converted to miniseed format for the next analysis stage.

We used the Python package MSNoise (Lecocq et al., 2014) to compute the crosscorrelations and measure the relative velocity changes. Only channel pairs with <60° vertical offset between boreholes were computed to encourage coherence of horizontally propagating waves. Records were band-pass filtered between 3000 and 4000 Hz to target high-frequency waves due to the close station offsets (<2 m). Power spectral density plots of the raw DAS data revealed a depth dependence only for frequencies <1000 Hz, suggesting that surface waves were only recorded at these lower frequencies and that the higher frequency arrivals were direct or scattered body waves (Figure 3a). The vertical orientation of the fiber-optic cable would have resulted in decreased sensitivity to horizontally propagating compressional waves (P-waves). Therefore, we suspect scattered vertically polarized shear waves (S-waves) as the primary phases in the crosscorrelations, and acoustic emissions as a likely source at this frequency range. We computed 1-minute crosscorrelations using the preprocessed records. Despite initial data-reduction efforts, the crosscorrelation procedure was still computationally intensive so we focused on measurements in the first 3 hours of each recording periods. We recognize omitting viable data is not desirable but needed to weigh the cost of computation time against correlation and measurement quality. The goal of this preliminary analysis was to determine if this methodological approach (DAS plus ambient noise) has potential for this application and warrants further study, for which 3 hours proved sufficient. A more in-depth study of the influence of stacking time and frequency is needed in the future.

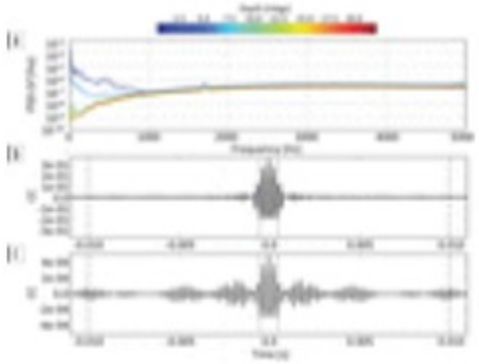

Figure 3. (a) The mean power spectral density (PSD) of raw poststimulation 1 DAS data from channels in the east hole as a function of depth. (b) Crosscorrelations (CC) are shown for channels 35 (20.262 m, west-4) and 100 (20.614 m, south-3) for the full 3-hour stack of crosscorrelations from prestimulation 1, and (c) an example 120-minute individual crosscorrelation from poststimulation 1. Measurements of $\delta v/v$ were made by comparing the delay time of the scattered phases as a function of lag time in a series of windows between the minimum and maximum lag times (dashed black lines), ±0.0005 s and ±0.01 s, respectively.

We stacked the 1-minute correlations into moving 120-minute stacks for each time period (prestimulation 1, poststimulation 1, prestimulation 2, poststimulation 2). Since this data set encompassed such small timescales and a unique time-period assessment compared to typical interferometry studies, the MSNoise source codes required significant alteration. We adjusted the MSNoise procedure to calculate velocity changes ($\delta v/v$) in sliding 120-minute stacks for each time period relative to the complete stack for prestimulation 1 (all 3 hours). Then, we averaged the individual $\delta v/v$ values for each channel pair in each time period. Figure 3 shows an example channel pair's full stack from prestimulation 1 and a representative poststimulation 1 individual 120-minute crosscorrelation. The $\delta v/v$measurements were done by calculating the phase delay (δt) between the two crosscorrelations in a series of overlapping windows (0.004 s wide) between minimum and maximum lag boundaries (±0.0005 s and ±0.01 s, respectively). The slope of the delay times as a function of lag time ($\delta t/t$) is equal to $-\delta v/v$ (Ratdomopurbo and Poupinet, 1995; Snieder et al., 2002; Clarke et al., 2011). This relationship contains the simplifying assumption that the velocity perturbation is homogeneous along the raypath.

$\delta v/v$ tomography. To better visualize the results and spatial variations, we computed a 3D tomographic inversion using the final $\delta v/v$ measurements for each station pair for poststimulation 1 and poststimulation 2. We used a Bayesian tomography approach and weighted each mean $\delta v/v$ measurement by its standard deviation. A 7 × 7 × 16 m volume was discretized into 0.5 × 0.5 × 0.5 m cells, centered on the test pad, and spanned the depth range of 8–24 m. Since the $\delta v/v$ measurements relied on scattered shear waves, we accounted for volumetric sensitivity by calculating the 3D Fresnel zone for each channel pair, assuming a 2000 m/s shear-wave velocity and 3500 Hz center frequency (0.57 m wavelength, λ). The Fresnel zone approximated the volume represented by each $\delta v/v$measurement, thereby accounting for

channels closer together sampling a smaller volume and thus having greater sensitivity to the localized velocity perturbations (i.e., fracture generation) than channels farther apart. This approximation also ensured greatest sensitivity near the channel locations (Figure 4) to be suitable for $\delta v/v$ inversion (Margerin et al., 2016).

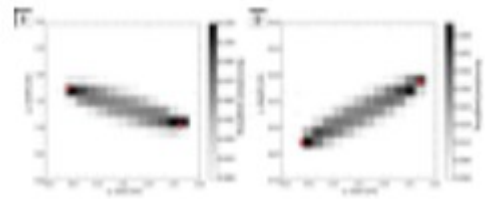

Figure 4.❸ An example normalized weighting function for channel pair 26-167 between the west and east holes. The weighting functions defined the zones of sensitivity for each channel pair in the $\delta v/v$ tomographic inversion.

For each channel pair, the straight-line path (L) between channel locations was found and divided into step segments (l) of 0.1 m. At each step increment (i), the Fresnel zone radius (r) was calculated by the following equation (Spetzler and Snieder, 2004):

$$r_i = \sqrt{\frac{n\lambda d_1 d_2}{L}}, \qquad ((1))$$

where d_1 and d_2 are the distances along the straight-line path to the current step location from the starting and ending channel locations, respectively, and n is a scalar (0.75 in this case). The radius was used to define a circle perpendicular to the straight-line path, then the area of the circle that fell within each intersecting cell (a_c) was calculated. These Fresnel zone areas were then normalized and summed along the entire straight-line path distance to get an integrated final weighting value (μ) for each cell (c) and channel pair (p) (Figure 4):

$$\mu_{c,p} = \sum_{i=0}^{L/l} \frac{\left(\frac{a_c}{\pi r_i^2}\right) * l}{L_p}. \qquad ((2))$$

We used a Markov Chain Monte Carlo (MCMC) algorithm to iteratively propose, accept, and reject models consisting of individual relative velocity variations for all cells (dv_{cells}). Following the sensitivity calculation, only 675 cells (out of 6272) ended up being used (intersected by a Fresnel zone) and active during the inversion. The volumetric sensitivity weights ($\mu_{c,p}$)

populated the matrix A (number of pairs × number of cells) and were used to take the modeled *dv* values of all cells and calculate predicted velocity variation measurements for each channel pair: $A \times dv_{cells} = dv_{pre}$. The MCMC algorithm ran for five chains, each of 1,000,000 iterations and starting with a model proposed at random from the prior *dv* distribution: $-15\% \leq dv \leq 10\%$. Cells were randomly chosen and perturbed per a Gaussian probability distribution centered at the current *dv* value with a variance of 0.5%. A proposed model was either accepted or rejected based on an acceptance criterion defined using the misfit between the predicted and observed velocity variations. Preliminary results were very scattered with large differences occurring between adjacent cells, which were either near zero or pushed toward the minimum and maximum *dv*boundaries. This suggested smoothing needed to be enforced, so we added a roughness calculation and factored the model roughness into the acceptance criterion. Therefore, models that reduced misfit and/or roughness were favored. An ensemble of the 25,0000 best (lowest misfit) models was created and used to find the final solution as the most probable *dv* value for each cell.

Crosshole seismic survey and tomography. In addition to the DAS measurements, we conducted angled crosswell seismic surveys before and after each stimulation. A pair of piezoelectric hydrophones (42 kHz center frequency, interchangeable as source and receiver) were lowered and raised incrementally within adjacent boreholes. The source hydrophone emitted compressional waves (P-wave) in the ultrasonic frequency band to be recorded on the receiver hydrophone in the adjacent hole, thereby providing a measurement of the subsurface P-wave velocity (V_P) between the two locations (Olson and Wright, 1989). A depth wheel controlled the hydrophone movements such that a signal was recorded every 1.4 cm along the entire length of the boreholes. The angled crosshole survey incorporated data from nine vertical offset angles between the source and receiver hydrophone (0°, ±15°, ±30°, ±45°, ±60°) for each borehole pair (six in total). These exhaustive campaigns resulted in more than 25,000 P-wave arrival picks used in a 3D tomographic inversion of each time-period (Knox et al., 2016). The tomographic images for the 2.44 × 2.44 × 12.2 m rectangular volume encompassing the experiment area were computed via an iterative least-squares inversion of the traveltimes subject to smoothing constraints. We found the raypath geometry for each time period using a Vidale-Hole finite-difference 3D eikonal solver (Vidale, 1990; Hole and Zelt, 1995). The vertical resolution was determined to be between approximately 7.5 and 15.2 cm from checkerboard tests (Knox et al., 2016).

RESULTS

Relative velocity changes (δv/v). All 120-minute crosscorrelation stacks were compared to the full 3-hour stack from prestimulation 1. Accordingly, the resulting average *δv*/*v* values for all stations pairs from prestimulation 1 were near zero (Figure 5). Following the first shot, the poststimulation 1 crosscorrelations overwhelmingly returned a relative velocity decrease. More

than 90% of station pairs recorded a velocity reduction, with an average reduction of −3% (Figure 5). Eighty-four percent of channel pairs measured a velocity decrease of −1% or more, 10% measured little to no velocity decrease ($-1\% < \delta v/v \leq 0\%$), and the remaining 6% of channel pairs showed a small velocity increase. The prestimulation 2 results were very similar to the poststimulation 1 results, but individual channel pairs did show some variation. The majority of poststimulation 2 crosscorrelations still showed a velocity reduction. Sixty-four percent of channel pairs measured a velocity decrease of −1% or more. Like poststimulation 1, 10% of channel pairs showed little to no velocity reduction compared to prestimulation 1 conditions. However, an increased number showed a relative velocity increase (20% of channel pairs) (Figure 5).

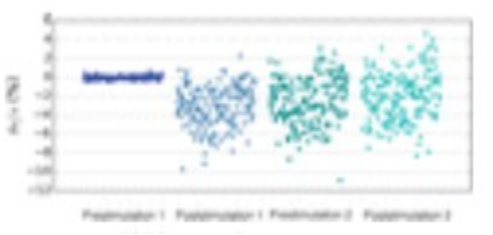

Figure 5.❸ Average percent velocity changes ($\delta v/v$) are shown as a function of channel pair and categorized by time period. All velocity changes are relative to the full 3-hour stack of prestimulation 1 crosscorrelations.

δv/v tomography. The 3D Bayesian tomography results for both poststimulation 1 and poststimulation 2 showed a velocity reduction throughout most of the experiment area. Contoured isosurface volumes revealed that the greatest reductions (~5%) were concentrated toward the center (Figure 6). The magnitude of velocity reduction increased toward the center stimulation hole and decreased toward the edges of the model area. Focusing on the largest magnitude velocity reductions, distinct zones were observed along the center, with variable morphology and orientations. Following poststimulation 1, zones of reduced velocity occurred from ~11 to 14 m, 15 to 18 m, and ~18 to 21 m depth. The shallow and deep zones appeared to strike approximately northeast to southwest, though the surfaces were fairly irregular (Figure 6). The greatest velocity reductions were near the center, from ~18 to 21 m depth, and slightly toward the southwest corner. Poststimulation 2 results were similar to poststimulation 1, where the magnitude of velocity reduction increased toward the center and distinct zones could be observed (Figures 6e–h). The greatest velocity reduction (>4%) following the second stimulation was concentrated at the greatest depths (~19–21 m). Smaller, secondary zones also occurred at ~17 m and at shallow depths (~12–13 m). Compared to poststimulation 1, the zones of reduced velocity become more spherical and less planar following the second stimulation.

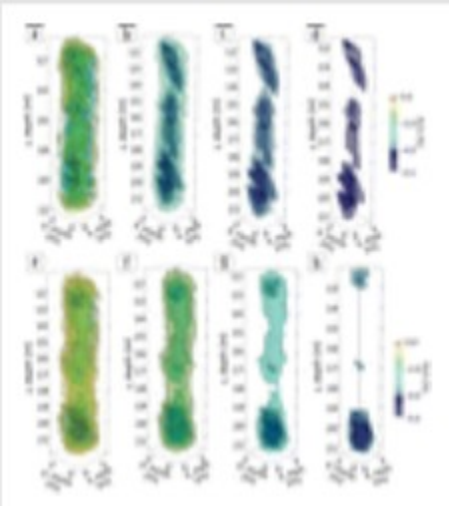

Figure 6. *δv*/*v* tomography results. Volumetric contours (isosurfaces) for poststimulation 1 are shown for the intervals (a) −1, −2, −3, −3.5, −4, and −4.5%; (b) −2, −3, −3.5, and −4%; (c) −3, −3.5, and −4; and (d) −3.5 and −4%. Poststimulation 2 isosurfaces are shown for the intervals (e) −1, −1.5, −2.25, −3, −3.5, and −4%; (f) −1.5, −2.25, −3, −3.5, and −4%; (g) −2.25, −3, −3.5, and −4%; and (h) −3, −3.5, and −4%.

P-wave tomography. We used the resulting V_P models from the CSL tomography to find the percent velocity change following each stimulation, relative to the first time period (prestimulation 1). Results showed both strong increases and decreases in V_P. Apart from some anomalies near the model edges, the greatest velocity reductions occurred near the center of the model area and slightly to the southwest (Figures 7a and 7c). Some heterogeneity in velocity variations was observed, with zones of large velocity increases present toward the model edges and in scattered zones between 10 and 15 m depth toward the eastern side. Contoured volumes showed variations with depth. Following stimulation 1, a semicontinuous zone of velocity reduction was seen throughout the model area concentrated toward the center and roughly oriented northeast to southwest. Velocity reductions appeared concentrated to the south and west at depths greater than ~18 m. Poststimulation 2 results were similar, except the zones of greatest velocity reduction were more segmented and spherical (Figure 7c). The magnitude of velocity changes also increased, in both positive and negative directions, following the second stimulation. Distinct shallow zones were observed in the center and slightly east above ~11 m, and in the southwest from 12 to 14 m. Velocity reduction was also concentrated in the center from 17 to 18 m with arms that extended and thinned to the south up to ~15 m and to the north down to ~21 m (Figure 7c). A second deep zone of great (>10%) velocity reduction was also observed near the south and west edges of the model, in a similar location as in poststimulation 1.

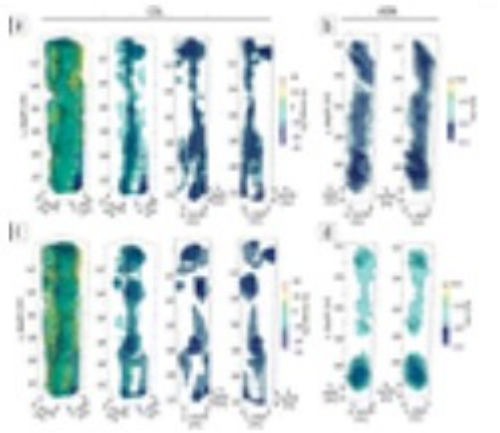

Figure 7. Comparison of tomographic results from CSL and ambient seismic noise $\delta v/v$ (ASN). (a) The CSL poststimulation 1 volumetric contours (isosurfaces) are shown for progressively fewer intervals from left to right: (10, 0, −10, −15, −20, and −25%), (−10, −15, −20, and −25%), and (−15, −20, and −25 %). The last interval range is shown looking west to east and then south to north. (b) ASN poststimulation 1 results for the −3, −3.5, and −4% isosurfaces, looking west to east and then south to north. (c) CSL poststimulation 2 isosurfaces for the intervals: (10, 0, −10, −15, −20, and −25%), (−10, −15, and −25%), and (−15 and −25 %), with the last interval range shown looking west to east and then south to north. (d) ASN poststimulation 2 results for −2.5, −3, −3.5, and −4% isosurfaces, looking west to east and then south to north.

Discussion

The greatest velocity reductions from the $\delta v/v$ tomography were concentrated around the center stimulation hole and generally supported the presence of a near-vertical fracture, as observed in downhole camera images (Figure 2b inset). Comparison of $\delta v/v$ tomography results with CSL tomography images revealed important similarities and differences, which were expected. First, both seismic methods returned velocity reductions near the stimulation borehole and emplaced fracture (center). Poststimulation 1 results for both methods showed reductions concentrated at depths greater than ~18 m and slightly toward the southwest corner of the array. This suggested fracturing was primarily at the depths corresponding to the energetic material emplacement, and dominant propagation was to the southwest. Second, both results showed a linear zone of velocity reduction that indicated the fracture was oriented roughly northeast to southwest and extended vertically throughout the model domain. However, the orientation was clearer in the crosshole results. The $\delta v/v$ results consistently showed the velocity reduction in the center while the crosshole results showed much more heterogeneity, including significant zones of velocity increases. Third, both methods revealed distinct zones of velocity reduction, including at shallow (12–14 m), intermediate (15–18 m), and deep (18–21 m) depths. For example, a discontinuity in the zones of greatest velocity reduction was observed around 14.5–15 m depth in both poststimulation 1 results (Figures 7a and 7b). Poststimulation 2 $\delta v/v$ images suggested the second stimulation primarily fractured around the center hole at deeper depths (~19–21 m) and to a lesser extent from 12–18 m (Figure 7d). The CSL results showed velocity reductions occurred separately at shallow (<14 m) and deep (>17 m)

depths, but both zones were less concentrated toward the center compared to the $\delta v/v$ results. In addition, the CSL results indicated greater fracturing between 17 and 18 m depth, with possible fracture limbs extending to shallower depths northward and deeper depths southward (Figure 7c). The $\delta v/v$ results did reveal a zone at 17–18 m depth that extended to shallower depths on the south side of the model. However, no northward extension below this volume was recovered, and the feature was secondary in terms of magnitude and size to the zone from 19–21 m depth. These differences could be the result of multiple factors including: (1) the CSL campaign used much higher frequencies than the $\delta v/v$ measurements, meaning they were sensitive to features at different scales; (2) the $\delta v/v$measurements used scattered waves and assumed a homogeneous velocity perturbation, which may in effect dampen or smear the velocity changes to a greater degree than can be accounted for with the inversion's volumetric sensitivity; and (3) the tomography in each case contained different smoothing parameters.

Conclusion

Preliminary results of relative velocity variations in seismic noise crosscorrelations from DAS show great promise for fracture detection and imaging. By using 3D Bayesian tomography that accounted for volumetric sensitivity, we were able to model spatial variations in $\delta v/v$ related to fracture emplacement. Velocity variations accurately located the emplaced fracture and characterized distinct zones in fracture morphology and orientation. Although crosshole seismic tomography should be examined at similar frequencies — so the wavefield is sensitive to similarly sized structures — the comparison supported the major $\delta v/v$ findings and helped validate this methodological approach. Three hours of ambient noise proved sufficient for obtaining meaningful measurements of velocity changes and spatial variations. The quality of these measurements is expected to improve with stacking time, so further analysis is needed to identify this method's full potential. Furthermore, the influence of frequency and wave type (body versus surface) should be explored to fully characterize the ambient wavefield. If lower frequencies prove useful in this type of imaging, lower sampling rates (<10 kHz) would greatly reduce the size of the data set and ease computation and memory requirements. The combination of DAS with ambient-noise techniques has great potential for large-scale characterization and monitoring studies with high-spatial and temporal resolution and relatively efficient and inexpensive data collection. We have shown that DAS can be used in conjunction with passive seismic interferometry techniques to detect and characterize fractured systems, and this methodological approach warrants further attention.

Acknowledgments

We want to thank Joe Greer, Thomas Coleman, and Ben Wygal at Silixa for help with the fiber-optic cable installation and DAS data collection. Thank you to Alex Prisjatschew, Eric Hass, and Michael Weathers from GTO; Traci

Rodosta, Andrea Dunn, Erik Albenze, and Kanwal Mahajan from NETL; Robert Abernathy at EMERTC; and Alex Rinehart at NMT. We would also like to acknowledge Kirsten Chojnicki, Zack Cashion, Greg Cieslewski, David Chavira, Adam Foris, and Doug Blankenship from SNL; Vince Vermeul and Chris Strickland from PNNL; Craig Ulrich, Pierpaolo Marchesini, Yuxin Wu, Tom Daley, and Paul Cook from LBNL; and Stewart Wehmeyer for helpful contributions to this project. Sandia National Laboratories is a multimission laboratory managed and operated by National Technology and Engineering Solutions of Sandia LLC, a wholly owned subsidiary of Honeywell International Inc. for the U.S. Department of Energy's National Nuclear Security Administration under contract DE-NA0003525.

References

1. Bergmann, P., M. Ivandic, B. Norden, C. Rücker, D. Kiessling, S. Luth, C. Schmidt-Hattenberger, and C.Juhlin, 2014, Combination of seismic reflection and constrained resistivity inversion with an application to 4d imaging of the CO2 storage site, Ketzin, Germany: *Geophysics*, 79, no. 2, B37–B50, https://doi.org/10.1190/geo2013-0131.1.

2. Berkowitz, B., 2002, Characterizing flow and transport in fractured geological media: A review: *Advances in Water Resources*, 25, no. 8–12, 861–884, https://doi.org/10.1016/S0309-1708(02)00042-8.

3. Brenguier, F., D. Clarke, Y. Aoki, N. M. Shapiro, M. Campillo, and V. Ferrazzini, 2011, Monitoring volcanoes using seismic noise correlations: *Comptes Rendus Geoscience*, 343, no. 8–9, 633–638, https://doi.org/10.1016/j.crte.2010.12.010.

4. Campillo, M., and A. Paul, 2003, Long-range correlations in the diffuse seismic coda: *Science*, 299, no. 5606, 547–549, https://doi.org/10.1126/science.1078551.

5. Chamberlin, R. M., 1981, Cenozoic stratigraphy and structure of the Socorro Peak volcanic center, central New Mexico: A summary: *New Mexico Geology*, 3, no. 2, 22–24.

6. Clarke, D., L. Zaccarelli, N. M. Shapiro, and F. Brenguier, 2011, Assessment of resolution and accuracy of the Moving Window Cross Spectral technique for monitoring crustal temporal variations using ambient seismic noise: *Geophysical Journal International*, 186, no. 2, 867–882, https://doi.org/10.1111/j.1365-246X.2011.05074.x.

7. Daley, T. M., B. M. Freifeld, J. Ajo-Franklin, S. Dou, R. Pevzner, V. Shulakova, S. Kashikar, D. E. Miller, J.Goetz, J. Henninges, and S. Lueth, 2013, Field testing of fiber-optic distributed acoustic sensing (das) for subsurface seismic monitoring: *The Leading Edge*, 32, no. 6, 699–706, https://doi.org/10.1190/tle32060699.1.

8. Day-Lewis, F. D., L. D. Slater, J. Robinson, C. D. Johnson, N. Terry, and D. Werkema, 2017, An overview of geophysical technologies appropriate for

characterization and monitoring at fractured-rock sites: *Journal of Environmental Management*, 204, no. Pt 2, 709–720, https://doi.org/10.1016/j.jenvman.2017.04.033.

9. Geertsma, J., and F. De Klerk, 1969, A rapid method of predicting width and extent of hydraulically induced fractures: *Journal of Petroleum Technology*, 21, no. 12, 1571–1581, https://doi.org/10.2118/2458-PA.

10. Hakami, E., and E. Larsson, 1996, Aperture measurements and flow experiments on a single natural fracture: *International Journal of Rock Mechanics and Mining Sciences & Geomechanics Abstracts*, 33, no. 4, 395–404, https://doi.org/10.1016/0148-9062(95)00070-4.

11. Hole, J., and B. Zelt, 1995, 3-D finite-difference reflection travel times: *Geophysical Journal International*,121, no. 2, 427–434, https://doi.org/10.1111/j.1365-246X.1995.tb05723.x.

12. James, S. R., E. J. Screaton, R. M. Russo, M. P. Panning, P. M. Bremner, A. C. Stanciu, M. E. Torpey, S.Hongsresawat, and M. E. Farrell, 2017, Hydrostratigraphy characterization of the Floridan aquifer system using ambient seismic noise: *Geophysical Journal International*, 209, no. 2, 876–889, https://doi.org/10.1093/gji/ggx064.

13. Johns, R. A., J. S. Steude, L. M. Castanier, and P. V. Roberts, 1993, Nondestructive measurements of fracture aperture in crystalline rock cores using X ray computed tomography: *Journal of Geophysical Research. Solid Earth*, 98, no. B2, 1889–1900, https://doi.org/10.1029/92JB02298.

14. Knox, H., J. Ajo-Franklin, T. Johnson, J. Morris, M. Grubelich, S. James, A. Rinehart, L. Preston, V. Vermeul, C. Strickland, J. Knox, D. King, and C. Ulrich, 2016, *Imaging fracture networks using joint seismic and electrical change detection techniques: Sandia National Laboratories Report Number: SAND2016-2001C*.

15. Lecocq, T., C. Caudron, and F. Brenguier, 2014, MSNoise, a python package for monitoring seismic velocity changes using ambient seismic noise: *Seismological Research Letters*, 85, no. 3, 715–726, https://doi.org/10.1785/0220130073.

16. Margerin, L., T. Planès, J. Mayor, and M. Calvet, 2016, Sensitivity kernels for coda-wave interferometry and scattering tomography: Theory and numerical evaluation in two-dimensional anisotropically scattering media: *Geophysical Journal International*, 204, no. 1, 650–666, https://doi.org/10.1093/gji/ggv470.

17. Molenaar, M. M., D. Hill, P. Webster, E. Fidan, and B. Birch, 2012, First downhole application of distributed acoustic sensing for hydraulic-fracturing monitoring and diagnostics: *SPE Drilling & Completion*, 27, no. 01, 32–38, https://doi.org/10.2118/140561-PA.

18. Moos, D., and M. D. Zoback, 1983, In situ studies of velocity in fractured crystalline rocks: *Journal of Geophysical Research. Solid Earth*, 88, no. B3, 2345–2358, https://doi.org/10.1029/JB088iB03p02345.

19. Moschetti, M. P., M. H. Ritzwoller, and N. M. Shapiro, 2007, Surface wave tomography of the western United States from ambient seismic noise: Rayleigh wave group velocity maps: *Geochemistry Geophysics Geosystems*, 8, no. 8, https://doi.org/10.1029/2007GC001655.

20. National Research Council, 1996, *Rock fractures and fluid flow: Contemporary understanding and applications*: National Academies Press.

21. Neal, J., and C. Krohn, 2012, Higher resolution subsurface imaging: *Journal of Petroleum Technology*, 64, no. 03, 44–53, https://doi.org/10.2118/0312-0044-JPT.

22. Neuman, S. P., 2005, Trends, prospects and challenges in quantifying flow and transport through fractured rocks: *Hydrogeology Journal*, 13, no. 1, 124–147, https://doi.org/10.1007/s10040-004-0397-2.

23. Olson, L. D., and C. C. Wright, 1989, Seismic, sonic, and vibration methods for quality assurance and forensic investigation of geotechnical, pavement, and structural systems, in H. L. M. dos Reis, ed., *Non-destructive testing and evaluation for manufacturing and construction*: Hemisphere Publishing Corporation, 263–278.

24. Parker, T., S. Shatalin, and M. Farhadiroushan, 2014, Distributed acoustic sensing — A new tool for seismic applications: *First Break*, 32, no. 2, 61–69, https://doi.org/10.3997/1365-2397.2013034.

25. Picozzi, M., S. Parolai, D. Bindi, and A. Strollo, 2009, Characterization of shallow geology by high-frequency seismic noise tomography: *Geophysical Journal International*, 176, no. 1, 164–174, https://doi.org/10.1111/j.1365-246X.2008.03966.x.

26. Ratdomopurbo, A., and G. Poupinet, 1995, Monitoring a temporal change of seismic velocity in a volcano: Application to the 1992 eruption of Mt. Merapi (Indonesia): *Geophysical Research Letters*, 22, no. 7, 775–778, https://doi.org/10.1029/95GL00302.

27. Sens-Schönfelder, C., and U. Wegler, 2006, Passive image interferometry and seasonal variations of seismic velocities at Merapi volcano, Indonesia: *Geophysical Research Letters*, 33, no. 21, https://doi.org/10.1029/2006GL027797.

28. Shapiro, N. M., and M. Campillo, 2004, Emergence of broadband Rayleigh waves from correlations of the ambient seismic noise: *Geophysical Research Letters*, 31, no. 7, https://doi.org/10.1029/2004GL019491.

29. Snieder, R., A. Grêt, H. Douma, and J. Scales, 2002, Coda wave interferometry for estimating nonlinear behavior in seismic velocity: *Science*, 295, no. 5563, 2253–2255, https://doi.org/10.1126/science.1070015.

30. Spetzler, J., and R. Snieder, 2004, The Fresnel volume and transmitted waves: *Geophysics*, 69, no. 3, 653–663, https://doi.org/10.1190/1.1759451.

31. Tsvankin, I., J. Gaiser, V. Grechka, M. Van Der Baan, and L. Thomsen, 2010, Seismic anisotropy in exploration and reservoir characterization: An overview: *Geophysics*, 75, no. 5, 75A15–75A29, https://doi.org/10.1190/1.3481775.

32. Verdon, J. P., J. M. Kendall, and A. Wüstefeld, 2009, Imaging fractures and sedimentary fabrics using shear wave splitting measurements made on passive seismic data: *Geophysical Journal International*, 179, no. 2, 1245–1254, https://doi.org/10.1111/j.1365-246X.2009.04347.x.

33. Vidale, J. E., 1990, Finite-difference calculation of travel times in three dimensions: *Geophysics*, 55, no. 5, 521–526, https://doi.org/10.1190/1.1442863.

34. Warpinski, N. R., and L. W. Teufel, 1987, Influence of geologic discontinuities on hydraulic fracture propagation (includes associated papers 17011 and 17074): *Journal of Petroleum Technology*, 39, no. 02, 209–220, https://doi.org/10.2118/13224-PA.